

Elevated V-ATPase Activity Following PTEN Loss Is Required for Enhanced Oncogenic Signaling in Breast Cancer



Amro H. Mohammad^{1,2}, Sung-Hoon Kim¹, Nicholas Bertos^{1,3}, Wissal El-Assaad^{1,2}, Ipshita Nandi^{1,2}, Harvey Smith¹, Jieyi Yang^{1,2}, Owen J. Chen^{1,2}, Isabelle Gamache¹, Trisha Rao^{1,2}, Bruno Gagnon⁴, Tina Gruosso^{1,3}, Michel L. Tremblay^{1,2}, Nahum Sonenberg^{1,2}, Marie-Christine Guiot^{1,5}, William Muller^{1,2}, Morag Park^{1,2,3,5,6}, and Jose G. Teodoro^{1,2}

ABSTRACT

PTEN loss-of-function contributes to hyperactivation of the PI3K pathway and to drug resistance in breast cancer. Unchecked PI3K pathway signaling increases activation of the mechanistic target of rapamycin complex 1 (mTORC1), which promotes tumorigenicity. Several studies have suggested that vacuolar (H⁺)-ATPase (V-ATPase) complex activity is regulated by PI3K signaling. In this study, we showed that loss of PTEN elevated V-ATPase activity. Enhanced V-ATPase activity was mediated by increased expression of the ATPase H⁺ transporting accessory protein 2 (*ATP6AP2*), also known as the prorenin receptor (PRR). PRR is cleaved into a secreted extracellular fragment (sPRR) and an intracellular fragment (M8.9) that remains associated with the V-ATPase complex. Reduced PTEN expression increased V-ATPase complex activity in a PRR-dependent manner. Breast cancer cell lines with reduced PTEN expression demonstrated

increased PRR expression. Similarly, PRR expression became elevated upon PTEN deletion in a mouse model of breast cancer. Interestingly, concentration of sPRR was elevated in the plasma of patients with breast cancer and correlated with tumor burden in HER2-enriched cancers. Moreover, PRR was essential for proper HER2 receptor expression, localization, and signaling. PRR knock-down attenuated HER2 signaling and resulted in reduced Akt and ERK 1/2 phosphorylation, and in lower mTORC1 activity. Overall, our study demonstrates a mechanism by which PTEN loss in breast cancer can potentiate multiple signaling pathways through upregulation of the V-ATPase complex.

Implications: Our study contributed to the understanding of the role of the V-ATPase complex in breast cancer cell tumorigenesis and provided a potential biomarker in breast cancer.

Introduction

Loss-of-function mutations of the tumor suppressor protein PTEN deleted on chromosome 10 occur in about 5% of human breast cancers (1). Epigenetic silencing of the *PTEN* gene or miRNA-mediated repression can also reduce expression of the PTEN protein in tumor cells contributing to oncogenicity (2). The major tumor suppressor activity of PTEN is to antagonize PI3K signaling by dephosphorylation of PIP₃ and thereby prevent Akt activation (3). Despite the relatively low mutation rate in breast cancer, tumors with mutant PTEN are an aggressive subtype with faster growth, earlier metastasis onset, and resistance to treatment (4, 5). In particular, treatment of HER2-positive breast

cancers with trastuzumab is ineffective in patients with low PTEN levels regardless of *PIK3CA* gene status (6, 7). Despite this understanding, the molecular basis of trastuzumab resistance after PTEN loss has yet to be elucidated.

Several studies have shown that the PI3K pathway is an important regulator of the vacuolar (H⁺)-ATPase (V-ATPase) complex (8–11). The V-ATPase complex is an ATP-driven proton pump that acidifies intracellular compartments including endosomes and lysosomes and is essential for a wide range of oncogenic signaling pathways (12). Notch receptor activation requires cleavage by pH-sensitive proteases in a V-ATPase-dependent mechanism (13). Similarly, V-ATPase-mediated endosomal acidification is critical for Wnt/β-Catenin signaling (14, 15). In addition to its functions in pH-dependent signaling pathways, the V-ATPase complex scaffolding functions are required for amino acid sensing, which is a prerequisite to mechanistic target of rapamycin complex 1 (mTORC1) activation and stimulation of mRNA translation (16). The V-ATPase promotes receptor internalization and ligand dissociation in clathrin-mediated endocytosis, which is essential to enhance signal transduction induced by a wide range of growth factor receptors (17–19). Loss of PTEN function in tumor cells could therefore have major effects on V-ATPase activity, which in turn would affect several oncogenic pathways. In HER2-positive breast cancer cells, for example, inhibition of the V-ATPase complex was shown to reduce membranous HER2 localization and signaling, and to overcome trastuzumab resistance (20).

Recently, we demonstrated that loss of PTEN in prostate cancer results in elevated expression of the ATPase H⁺ transporting accessory protein 2 (encoded on *ATP6AP2*), which is also known as the prorenin receptor (PRR; ref. 21). PRR is a 350-amino acid protein with

¹Goodman Cancer Research Centre, McGill University, Montreal, Quebec, Canada. ²Department of Biochemistry, McGill University, Montreal, Quebec, Canada. ³Molecular Oncology Group, McGill University Health Centre, Montreal, Quebec, Canada. ⁴Department of Family Medicine and Emergency Medicine, Laval University, Laval, Quebec, Canada. ⁵McGill University Health Centre, McGill University, Montreal, Quebec, Canada. ⁶Department of Oncology, McGill University, Montreal, Quebec, Canada.

Note: Supplementary data for this article are available at Molecular Cancer Research Online (<http://mcr.aacrjournals.org/>).

Corresponding Author: Jose G. Teodoro, McGill University, 1160 Pine Avenue, Cancer Pavilion Room 604, Montreal, Quebec H3A 1A3, Canada. Phone: 514-398-3273; Fax: 514-398-6769; E-mail: jose.teodoro@mcgill.ca

Mol Cancer Res 2020;18:1477–90

doi: 10.1158/1541-7786.MCR-20-0088

©2020 American Association for Cancer Research.

one transmembrane domain that is proteolytically cleaved into two fragments in the trans-Golgi network (22, 23). The N-terminal 28-kDa fragment, called soluble PRR (sPRR), is secreted and can be detected in blood and urine (22, 24). sPRR is believed to have a role in the renin-angiotensin system by mediating the processing of prorenin to renin (23). The C-terminal fragment of PRR, designated M8.9, remains associated with the V-ATPase and is critical for V-ATPase assembly and function (15, 25–28). Consistent with its essential role as a V-ATPase cofactor, the *ATP6AP2* gene is ubiquitously expressed in mammalian tissues (29). In addition, *Atp6ap2*-knockout mouse embryos die early in development, and conditional deletion in adult animals results in death through multiple organ failure (30, 31). Although the PI3K pathway clearly plays a role in regulating the V-ATPase complex (32), the effects of PTEN loss on the V-ATPase complex have never been addressed.

We show here that low PTEN expression in breast cancer cells resulted in elevated *ATP6AP2* expression and sPRR secretion. Furthermore, reduced levels of PTEN promote higher V-ATPase activity, which is dependent on PRR expression. Analysis of blood plasma from patients with breast cancer showed elevated sPRR concentration compared with healthy subjects and a positive correlation between sPRR concentration and tumor volume in patients with HER2-enriched tumors. Knockdown of PRR reduced HER2 expression, localization, and signaling in HER2-positive breast cancer cells. In the same cells, PRR knockdown also decreased mTORC1 activity. Our data suggest that PTEN negatively regulates PRR expression and V-ATPase complex activity in breast cancer cells, and the loss of this regulation enhances multiple oncogenic signaling pathways.

Materials and Methods

Cell culture, cell lines, and drugs

All human cell lines used in this study were obtained from the ATCC and used at an early passage in 2013 and 2014 after expansion. ATCC cell line authentication procedures include karyotyping, morphology examination, cytochrome C oxidase I gene analysis, and short tandem repeat profiling. At the onset of the study, cell lines were tested for *Mycoplasma* contamination using MycoAlert (Lonza, LT07-118) or conventional DAPI staining. *Mycoplasma* testing would then be conducted as needed throughout the study. Cells were used, on an average, to a passage number of 10–12 before being discarded. The cell lines MCF-7 (RRID: CVCL_0031), T47-D (RRID: CVCL_0553), BT549 (RRID: CVCL_1092), HCC 1395 (RRID: CVCL_1249), HCC 1569 (RRID: CVCL_1255), and HCC 70 (RRID: CVCL_1270) were cultured in RPMI1640 1× (Wisent, 350-000-CL). Cell lines BT474 (RRID: CVCL_0179), SKBR3 (RRID: CVCL_0033), MDA-MB 453 (RRID: CVCL_0418), MDA-MB/UACC 893 (RRID: CVCL_1782), MDA-MB 157 (RRID: CVCL_0618), HS578T (RRID: CVCL_0332), MDA-MB 231 (RRID: CVCL_0062), MDA-MB 361 (RRID: CVCL_0620), and MDA-MB 468 (RRID: CVCL_0419) were cultured in DMEM 1× (Wisent, 319-005-CL). MDA-MB 436 cells (RRID: CVCL_0623) were cultured in Leibovitz's L15 (Wisent, 323-050-CL). MCF-7 *PTEN*sh/scrambled cells were maintained with 1 µg/mL puromycin in RPMI1640 1×. All culture media were supplemented with 50 µg/mL Gentamycin Sulfate (Wisent, 450-135-XL) and 10% FBS (Sigma-Aldrich, #F1051-Canadian Origin). All cell lines were trypsinized with 0.25% Trypsin/EDTA (Wisent, 325-043-CL) except for lines HCC 1395, 1569, and 70, which were trypsinized with 0.05% Trypsin/EDTA (Invitrogen, 25300054). Bafilomycin A1 (88899-55-2) was purchased from Sigma. Trastuzumab (Herceptin) was obtained from Genentech, Inc.

Cell lysis, protein quantification, and protein precipitation

Cell lysis was performed using NP-40 lysis buffer (0.5% NP-40, 50 mmol/L Tris-hydrochloric acid, and 150 mmol/L sodium chloride) supplemented with 50 mmol/L Sodium Fluoride, 10 mmol/L Glycerol-2-Phosphate, 100 µmol/L Sodium Orthovanadate, and Protease Inhibitor Tablet (Roche, 04693124001). Protein quantification of lysates was performed using the Bradford Protein Assay (Bio-Rad, 5000-00-6). Protein quantification of secreted proteins in conditioned media was performed using the 2-D Quant Kit (GE Healthcare, 121405). Secreted proteins were precipitated from serum-free, ITS-supplemented media by trichloroacetic acid (TCA) precipitation. Conditioned media was brought to a final concentration of 0.1% sodium lauryl sarcosinate using a 10% stock solution. After a 2-minute incubation at room temperature, 100% TCA was added to a final concentration of 15% (volume/volume). Samples were vortexed for 5 seconds and incubated on ice for 2 hours. Samples were then centrifuged at 10,000 × *g* for 10 minutes at 4°C, the supernatant was discarded, and the pellet was washed with ice-cold acetone. This procedure was repeated twice. Pellets were dried completely, dissolved in urea buffer [7 mol/L urea, 2 mol/L thiourea, 4% (w/v) CHAPS, and 30 mmol/L Tris], and incubated on a shaker at 600 rpm overnight at room temperature.

Antibodies, Western blotting, and band quantification

Rabbit monoclonal anti-PTEN (138G6, #9559), anti-Thr308 phosphorylated Akt (#9257), Tyr1221/1222 phosphorylated HER2/ErbB2 (#2249), HER2/ErbB2 (D8F12, #4290), anti-Thr389 phosphorylated P70-S6K (#9205), Thr202/Tyr204 phosphorylated p44/42 MAPK (ERK1/2) (#9101), and p44/42 MAPK (ERK1/2) (#9102) antibodies were obtained from Cell Signaling Technology. Rabbit polyclonal anti-total P70S6K (C-18) antibody (sc-230) was purchased from Santa Cruz Biotechnology (prior to 2016). Rabbit polyclonal anti-PRR [N3C3] (GTX114169) was purchased from GeneTex. Rabbit polyclonal anti-PRR (Ab40790) was purchased from Abcam for detection of human PRR on tissue microarrays (TMA). Rabbit polyclonal anti-PRR (Ab64957) was also purchased from Abcam for IHC detection of murine PRR. Western blotting was conducted using TGX Stain-Free Technology (Bio-Rad). Gels were made using the TGX Stain-Free FastCast Acrylamide Kit, 12% (Bio-Rad, 161-0185). Protein transfers were performed on the Turbo Blot Transfer Apparatus (Bio-Rad-7 min TURBO protocol) using the Transblot Turbo TRA transfer kit with low fluorescence polyvinylidene difluoride membranes to minimize background noise (Bio-Rad, 1704275). Blocking was done using standard nonfat powder milk 5% (w/v) in TBS-T [50 mmol/L Tris (pH 7.5), 150 mmol/L NaCl, and 0.5% Tween 20]. Blots were exposed to Clarity Western ECL (Bio-Rad, 1705061) or SuperSignal™ West Femto (Thermo Fisher Scientific, 34095) for band visualization with a Chemidoc XRS+ System (Bio-Rad) using the “high resolution chemiluminescence” protocol. Finally, bands were quantified using Image Lab 5.1 Software (Bio-Rad). Band intensity was measured using the “Lane and Bands” tool and then normalized to the “stain-free blot” containing the total protein lanes using the “Multichannel” feature (33, 34).

qRT-PCR

Breast cancer cells were plated on 60 mm dishes and incubated until 70%–90% confluence was reached. Cells were then conditioned with serum-free media supplemented with 1× insulin, transferrin, and selenium (ITS) overnight. Total RNA was extracted the next day using TRIzol (Invitrogen). One microgram of RNA was reverse transcribed to cDNA (QuantiTect Reverse Transcription Kit, Qiagen). qRT-PCR analysis was performed on the Eppendorf realplex system

using the QuantiFast SYBR Green PCR Kit (Qiagen). Gene expression analysis was determined using the ΔC_t method normalized to Cyclophilin. Primer sequences are listed in Supplementary Table S3.

PTEN reconstitution via adenovirus infection

PTEN and LacZ adenovirus (Ad) constructs were described previously (21). Virus titer was assessed using the fluorescence-forming unit protocol as described previously (35). Cells were seeded at a density of 4.0×10^5 cells per well in 6-well plates 24 hours prior to infection. Infections with LacZ-Ad or PTEN-Ad were done at a multiplicity of infection of 100. Twenty-four hours after infection, media were replaced with serum-free media supplemented with $1 \times$ ITS and conditioned for 16–20 hours. Conditioned media were collected for protein precipitation and cells were lysed for Western blot analysis as described above.

Neo MMTV-ErbB2 mouse model production and tissue processing

The MMTV-ErbB2 mouse model (Neu NT/MMTV) was described previously (36). The MMTV promoter in this model drives expression of Neu and Cre recombinase (37). Subsequently, these mice were crossed with Flox-*Pten* mice (129/J, The Jackson Laboratory) to create *Pten*^{+/-} and *Pten*^{-/-} mice. Genotype validation was conducted by PCR as reported previously (38, 39). RNA and protein were extracted from the breast tumors using the ALLPrep DNA/RNA/Protein Mini Kit (ref. 40; Qiagen, 80004). Four micrometer sections from the same tumors were obtained and stained for PRR expression.

siRNA transfection and short hairpin RNA infection

MCF-7 cells were seeded at a density of 2.0×10^5 cells per well in a 6-well plate. Cells at 50% confluency were then transfected with 50 nmol/L of each PRR siRNAs, or nonsilencing siRNA (Sigma) using 5 μ L Lipofectamine 2000 (Sigma) per well for 4 hours. Analyses were performed 24 hours following transfection. For stable knockdown of PRR, PRR shRNA-pLKO vectors or pLKO vector was transfected in HEK 293T-17 (ATCC #CRL:11268) for virus production along with lentivirus packaging plasmids pCMV-dR8.2 and pCMV.VSV.G (Addgene). Supernatant from HEK 293T-17 cells was collected 48 hours following transfection, with 8 μ g/mL Polybrene (Sigma), and was used to infect target MDA-MB 231 cells. PRR-knockdown cells were selected for using 1 μ g/mL puromycin for 72 hours. PRR siRNA and short hairpin RNA (shRNA) sequences used are listed in Supplementary Table S3.

V-ATPase activity and proliferation assays

Cells were seeded at a density of 2.0×10^5 cells per well in 6-well plates. After reaching 50% to 60% confluency, cells were incubated at 37°C and 5% CO₂ with 100 nmol/L LysoTracker Red DND-99 (Invitrogen, L7528) in fresh complete medium for 50 minutes in the dark. Cells were then washed twice with PBS $1 \times$ and incubated with fresh complete media for 10 minutes at 37°C and 5% CO₂ prior to imaging. Both brightfield and fluorescence images were captured using a Zeiss Axiovert Fluorescence Microscope (20 \times objective). For Bafilomycin A1 treatments, cells were exposed to 100 nmol/L Bafilomycin A1 for 1 hour prior to incubating cells with the LysoTracker indicator. To quantify LysoTracker signal per cell, cells in brightfield images were manually counted using the “Cell Counter” plugin from ImageJ. Gray scales of fluorescence images were adjusted for a minimum of 50 and maximum of 255 using the “brightness/contrast” option. The mean gray value of each image was then measured as optical density (OD) units and divided over the number of cells to estimate the LysoTracker

signal per cell. Values were then divided over corresponding control counterparts to calculate percentage values relative to control treatment.

In the proliferation assay, MDA-MB 231 cells infected with PRR shRNA 1 or shRNA 2 were seeded at a density of 1.0×10^5 cells per well in a 6-well plate and placed directly into the IncuCyte Imaging System (Sartorius) to analyze proliferation. The “phase-contrast” protocol was chosen to measure proliferation by analyzing occupied area (% confluence) of cell images in real-time over 48 hours. Cells were then harvested and analyzed to validate knockdown of PRR.

TMA, The Cancer Genome Atlas PRR mRNA levels, and laser capture microdissection

TMA were constructed from clinical formalin-fixed, paraffin-embedded blocks obtained from the McGill University Health Centre (MUHC, Montreal, Quebec, Canada) breast tissue bank. Cores (2 \times 1 mm) were present on the TMA for each patient (Supplementary Table S1A and S1B). TMA blocks were sectioned at 4 μ m thickness. TMAs were pretreated with DIVA (DV2004) for antigen retrieval at 125°C for 10 minutes. The TMAs were then blocked with enzyme block (S2003) and Protein Block Serum-Free (X0909) purchased from Dako for 15 minutes. TMAs were then incubated with PRR antibody (Ab40790) or P-Akt (Thr 308; Cell Signaling Technology #9257) at 1:1,000 dilution in 5% BSA for 1 hour and then with 1:500 goat anti-rabbit secondary antibody (The Jackson Laboratory, 111-035-144). The chromogen used was DAB (Dako, K3468) and counterstaining was done using HemaTox (Leica, 3801698). After imaging, TMAs were scored for PRR or P-Akt staining (0, no staining; 1, weak staining; 2, moderate staining; and 3, strong staining). Three independent observers scored the TMA for each subject. The final staining score for each subject was the average of these three measurements.

Bioinformatics analysis of PRR expression in human breast carcinomas was performed by extracting data from The Cancer Genome Atlas (TCGA) database. Using the GEPIA2 interface, we investigated the expression levels of PRR from the TCGA breast invasive carcinoma cohort (BRCA; $n = 1,215$ tumors; ref. 40; <http://gepia2.cancer-pku.cn/>). RNA-Seq Expectation by Maximization (RSEM) normalized counts were extracted for the PRR gene (*ATP6AP2*) and assessed for percentile data classification (high, top 25% and low, bottom 25%). Subsequently, recurrence-free survival data was generated by Kaplan–Meier survival analysis for Luminal A, Luminal B, HER2-enriched, and Basal patients stratified on the basis of PRR expression levels. Significance was calculated by log-rank Mantel–Cox test for statistical difference in recurrence-free survival between “high” and “low” *ATP6AP2* expression groups. Laser capture microdissection (LCM), RNA extraction, linear amplification, and microarray hybridization protocols were done as detailed previously (41).

sPRR ELISA

Plasma was collected from patients with breast cancer and from healthy women (Supplementary Table S2). Plasma samples from patients with breast cancer were collected from a cohort at the MUHC (Montreal, Quebec, Canada). Plasma samples from healthy women were obtained from a biobank established for biomedical and epidemiologic research on patients with cancer at McGill University (Montreal, Quebec, Canada, Supplementary Table S2). All samples collected were aliquoted and stored at -80°C until further use. Quantitative determination of sPRR levels in the plasma of patients with breast cancer was performed by ELISA using the manufacturer’s protocols (IBL International, JP27782). Plasma samples were diluted

8-fold prior to conducting the ELISA to stay within linear range of the ELISA.

Immunostaining and fluorescence

A total of 50,000 SKBR3 or MDA-MB 893 cells were plated on circular Fisherbrand microscope cover glass (12-545-81) placed in 12-well plates. Fixation was carried out using 2% paraformaldehyde for 10 minutes at room temperature. Cells were then permeabilized using 0.2% Triton X-100 for 20 minutes at room temperature. For blocking, 2% BSA in wash buffer (1× PBS with 0.2% Triton and 0.05% Tween-20) was used for 1 hour at room temperature. Coverslips were then incubated with primary antibodies for HER2 (D8F12, Cell Signaling Technology, 1:100) and PRR (GTX11419, GeneTex, 1:100) in blocking buffer for 1 hour at room temperature. Following a three-round rinse with wash buffer, coverslips were incubated with Alexa Fluor 647 Donkey anti-Mouse (IgG) for HER2 (ab150107, Abcam) and Alexa Fluor 555 Donkey anti-Rabbit (IgG) for PRR (ab150074, Abcam) 1:1,000 secondary antibodies. Cells were then rinsed three times and stained with 0.5 ng/mL 4',6-diamino-2-phenylindole (DAPI) for 5 minutes at room temperature for nuclear staining. Coverslips were mounted using Embedding Medium (Tissue Tek, 4583) and allowed to dry overnight before imaging. Images were taken using the LSM 710 Zeiss Confocal Microscope. Images were then processed using FIJI (Image J) Software to measure HER2 immunoreactivity and examine HER2 localization. HER2 expression was calculated relative to the staining area measured to accurately compute intensity of staining. Percentage of membranous HER2 staining was calculated on the basis of the number of cells that expressed HER2 at the membrane relative to total number of cells in each field.

Polysome profiling

At least 15×10^6 cells plated in 15 cm petri dishes were treated with cycloheximide (100 µg/mL) in growth media for 5 minutes at 37°C and 5% CO₂ to immobilize ribosomes translating mRNAs. Cells were washed twice and scraped using ice-cold 1× PBS containing cycloheximide. Cells were then centrifuged at $200 \times g$ for 5 minutes at 4°C and supernatants were discarded. Cells were then resuspended in 425 µL of hypotonic buffer [5 mmol/L Tris-HCl (pH 7.5), 2.5 mmol/L MgCl₂, 1.5 mmol/L KCl, and 1× protease inhibitor cocktail (EDTA-free)], in addition to 5 µL of 10 mg/mL cycloheximide, 1 µL of 1 mol/L DTT, and 100 U of RNase inhibitor (NEB #M0307). Mixture was then vortexed for 5 seconds followed by addition of 25 µL of 10% Triton X-100 (final concentration 0.5%) and 25 µL of 10% sodium deoxycholate (final concentration 0.5%). Samples were then vortexed for an additional 5 seconds. To obtain the cytosolic fraction, a mild hypotonic buffer was used to cause cell swelling and rupture while keeping the nuclear envelope intact. Lysates were then centrifuged at $16,000 \times g$ for 7 minutes at 4°C and supernatants were transferred to new prechilled tubes. OD at 260 nm was measured for each sample and supernatants were loaded into prechilled ultracentrifuge tubes containing sucrose gradient (5%–50%) after adjusting lysates to nearly the same OD (10–20 OD at 260 nm) in lysis buffer. Samples were then centrifuged at $222,228 \times g$ for 2 hours at 4°C. Tubes were then carefully removed from the rotor and placed on ice. Ultracentrifuge tubes were then positioned to start the upward displacement of the sucrose gradient while simultaneously measuring absorbance at 254 nm of each fraction.

Ethics

The mouse work conducted in this study was approved by McGill University Animal Care Committee (animal use protocol #5518).

Patients were provided with a written informed consent under MUHC Research Ethics Board–approved protocols SDR-990780 and SDR-00-966.

Statistical analysis

GraphPad Prism (version 6) was used for statistical analyses. Data are presented as mean ± SD. *N* number represents independent biological repeats. Student *t* tests were used for two group comparisons. Correlations were assessed by computing Pearson correlation coefficient. Statistical significance for TCGA scatter whisker and box plots was measured using Bonferroni multiple comparison test. For Kaplan–Meier curves, statistical significance was assessed using the log-rank (Mantel–Cox) test. *, $P \leq 0.05$; **, $P \leq 0.01$; ***, $P \leq 0.005$; and ****, $P < 0.0001$ indicate differences that were considered statistically significant.

Results

PTEN regulates PRR expression and sPRR secretion in multiple breast cancer lines and in a mouse model of breast cancer

We previously reported an increase in the expression of PRR in prostate cancer tissue compared with normal tissue in a PTEN-dependent manner (21). Analysis of gene expression data from TCGA revealed that PRR mRNA levels were also elevated in breast cancer tissue, suggesting a similar relationship may exist between PTEN and PRR in breast cancer tissue (Supplementary Fig. S1). To further study the relationship between PTEN and PRR, 14 breast cancer cell lines, representing each of the molecular subtypes, were tested by immunoblot analysis for PTEN and PRR expression and sPRR secretion (Fig. 1A). Although PTEN mutations are present in only 5% of breast cancers, we observed a wide range of PTEN expression levels consistent with previous studies showing epigenetic regulation of PTEN (2). The cell lines were categorized into “high” or “low” PTEN expression groups (Fig. 1B and C). We observed that sPRR secretion was significantly increased in lines where PTEN expression was reduced or absent (Fig. 1B and C). qRT-PCR analysis of PRR expression in the 14 cell lines also revealed a significant increase in PRR mRNA in PTEN “low” expression lines compared with PTEN “high” expression lines (Fig. 1D and E). To further confirm the role of PTEN in the regulation of sPRR secretion, PTEN was stably knocked down in MCF-7 cells (*PTEN*^{sh} MCF-7). *PTEN*^{sh} MCF-7 cells secreted significantly more sPRR than their scrambled controls (Fig. 1F and G). Similarly, reconstitution of PTEN in PTEN-null BT549 or MDA-MB 468 using an adenovirus vector resulted in a significant reduction in sPRR secretion in comparison with control LacZ infection (Fig. 1F and G). Together, these data indicate that PTEN expression controls both PRR expression and PRR processing to sPRR.

We then tested the relationship between PTEN and PRR in a mouse model of breast cancer. Breast-specific deletion of PTEN in the ErbB2-overexpressing mouse model has been shown to accelerate tumor formation and angiogenesis (4). PRR expression was analyzed in the *Pten*^{+/+} and *Pten*^{-/-} Neo Neu/NT MMTV mice. Immunostaining of sections from both genotypes revealed higher PRR/sPRR staining in *Pten*^{-/-} Neo Neu/NT MMTV mouse sections compared with PTEN wild-type controls (Fig. 1H). Immunoblot analysis of protein extracted from tumors also revealed a significant increase in PRR levels in *Pten*^{-/-} tumors (Fig. 1I and J). Together, our findings demonstrate a relationship between PTEN and PRR expression/processing in breast cancer.

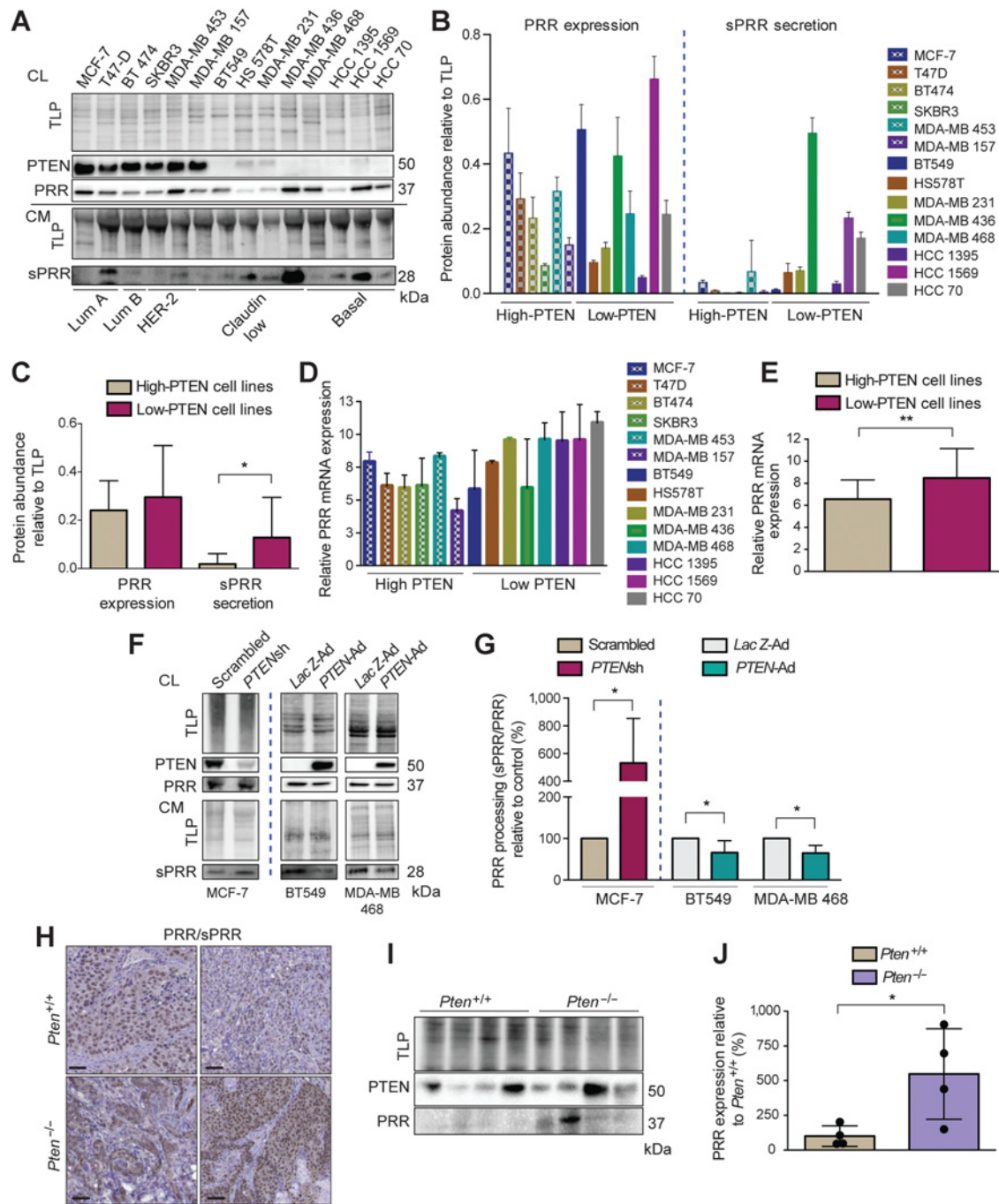


Figure 1. PTEN regulates PRR expression and sPRR secretion in multiple breast cancer lines and in a mouse model of breast cancer. **A**, Western blot analysis of PTEN and PRR protein levels in cell lysates (CL), and of sPRR levels in conditioned media (CM) of 14 breast cancer cell lines grouped according to PTEN “high” or “low” expression. **B**, Corresponding quantification of PRR expression and sPRR secretion relative to total lane protein (TLP) across the PTEN “high” or “low” cell lines ($n = 3$). **C**, Quantification of average PRR expression and sPRR secretion relative to TLP across PTEN “high” or “low” cell lines. **D**, Quantification of PRR qPCR analysis across the PTEN “high” or “low” cell lines. **E**, Quantification of average PRR expression across PTEN “high” or “low” cell lines. **F**, Western blot analysis of PRR and sPRR in control (scrambled) and PTEN-knockdown (*PTENsh*) MCF-7 cells, and in *LacZ-Ad*- or *PTEN-Ad*-infected PTEN-null breast cancer cell lines BT549 and MDA-MB 468. **G**, Quantification of PRR processing assessed by computing the ratio for the secretion of sPRR relative to expression of full-length PRR (sPRR/PRR) in *PTENsh* MCF-7 relative to scrambled ($n = 4$), in *PTEN-Ad*-infected BT549 relative to *LacZ* ($n = 4$), and in *PTEN-Ad*-infected MDA-MB 468 relative to *LacZ* ($n = 5$). **H**, Representative PRR/sPRR IHC images of breast cancer tumor sections obtained from *Pten*^{+/+} and *Pten*^{-/-} Neo Neu/NT MMTV mice (magnification, 40 ×; scale bar, 100 μm). **I**, PRR expression is elevated in Neo Neu/NT MMTV Cre mice breast tissue after PTEN loss as demonstrated in Western blot analysis of PRR expression in lysates of mammary tumors obtained from *Pten*^{+/+} and *Pten*^{-/-} Neo Neu/NT MMTV mice. **J**, Corresponding quantification of PRR expression in *Pten*^{-/-} ($n = 4$) compared with *Pten*^{+/+} Neo Neu/NT MMTV tumors. Lum A, Luminal A; Lum B, Luminal B; *, $P \leq 0.05$; **, $P \leq 0.01$.

Downloaded from <http://aacrjournals.org/mcr/article-pdf/18/10/1477/2190679/1477.pdf> by McGill University user on 08 September 2022

PTEN knockdown causes elevated V-ATPase activity that can be reversed by PRR knockdown

We next determined whether the regulation of PRR by PTEN is able to modulate V-ATPase complex activity. *PTENsh* MCF-7 cells have increased V-ATPase activity compared with scrambled

controls as measured by vesicular acidification (LysoTracker staining; Fig. 2A-C; Supplementary Fig. S2A). As shown above in Fig. 1, *PTENsh* MCF-7 cells also display slightly elevated expression of PRR. To determine the role that elevated PRR may have on V-ATPase activity, we knocked down PRR in scrambled

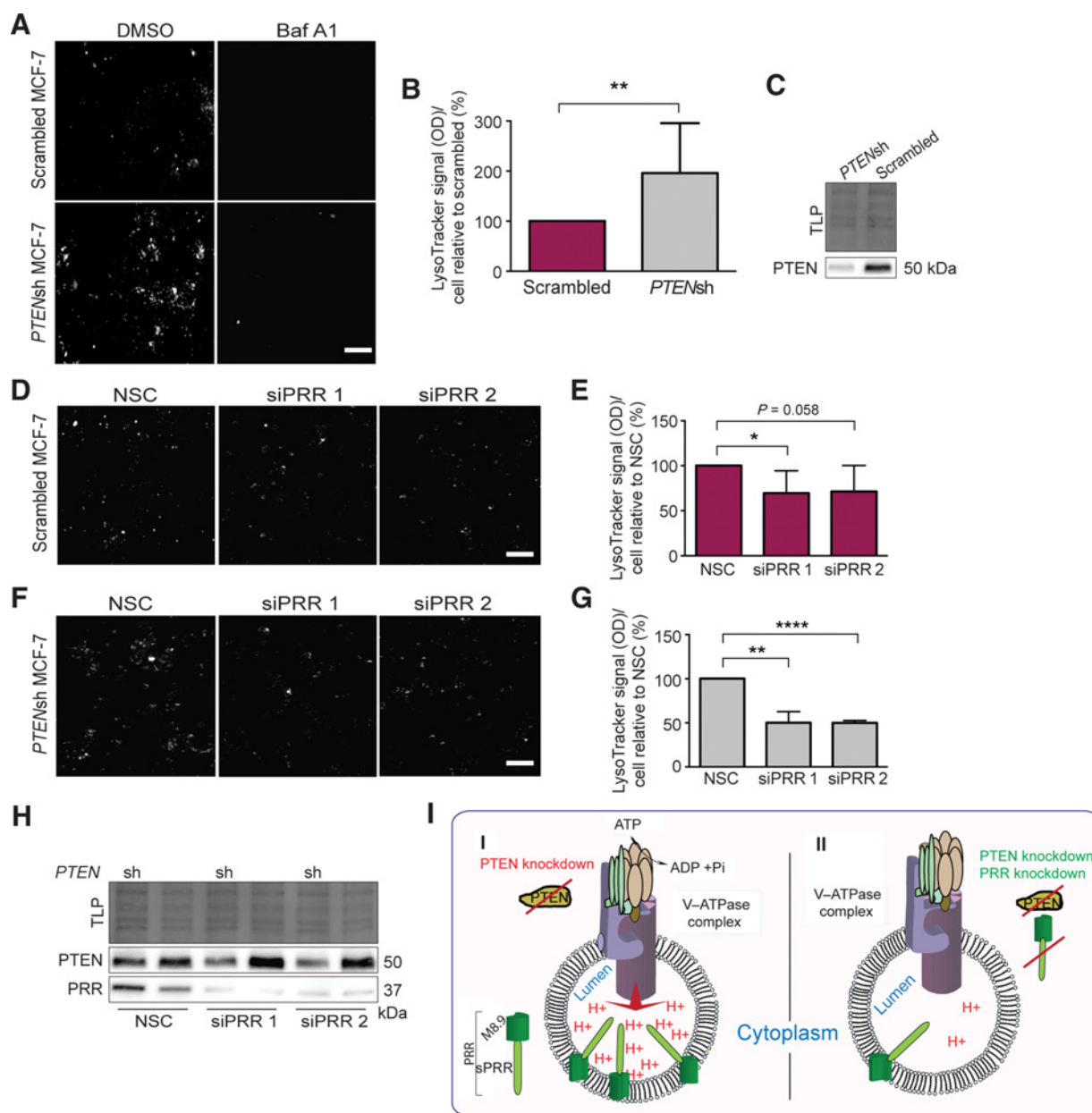


Figure 2. PTEN knockdown causes elevated V-ATPase activity that can be reversed by PRR knockdown. **A**, Representative LysoTracker images of PTEN-knockdown (*PTENsh*) and scrambled MCF-7 cells treated with DMSO or Bafilomycin A1 (Baf A1; 100 nmol/L). Treatment with Bafilomycin A1 is included as a positive control for V-ATPase inhibition. **B**, Corresponding quantification of LysoTracker signal as mean gray value (OD) per MCF-7 cell infected with *PTENsh* shRNA relative to scrambled MCF-7 cells ($n = 7$). **C**, Western blot analysis of PTEN showing a reduction in PTEN expression after PTEN knockdown. **D**, Representative LysoTracker images of control scrambled MCF-7 cells transfected with nonsilencing control (NSC), or two different siRNAs targeting PRR (siPRR 1 and 2). **E**, Corresponding quantification of LysoTracker signal of control scrambled MCF-7 cells transfected with NSC, siPRR 1, or siPRR 2 relative to NSC ($n = 5$). **F**, Representative LysoTracker images of *PTENsh* MCF-7 cells transfected with NSC, siPRR 1, or siPRR 2 relative to NSC ($n = 3$). **G**, Corresponding quantification of LysoTracker signal of *PTENsh* MCF-7 cells transfected with NSC, siPRR 1, or siPRR 2 relative to NSC ($n = 3$). **H**, Western blot analysis of PTEN and PRR in *PTENsh* and scrambled MCF-7 cells after transfection with NSC, siPRR 1, or siPRR 2. **I**, Schematic showing active V-ATPase complex when PTEN is knocked down (I) and inactive V-ATPase complex when PTEN and PRR are knocked down (II). Scale bar, 100 μ m on 20 \times images. Corresponding brightfield images can be found in Supplementary Fig. S2. TLP, total lane protein; *, $P \leq 0.05$; **, $P \leq 0.01$; ****, $P < 0.0001$.

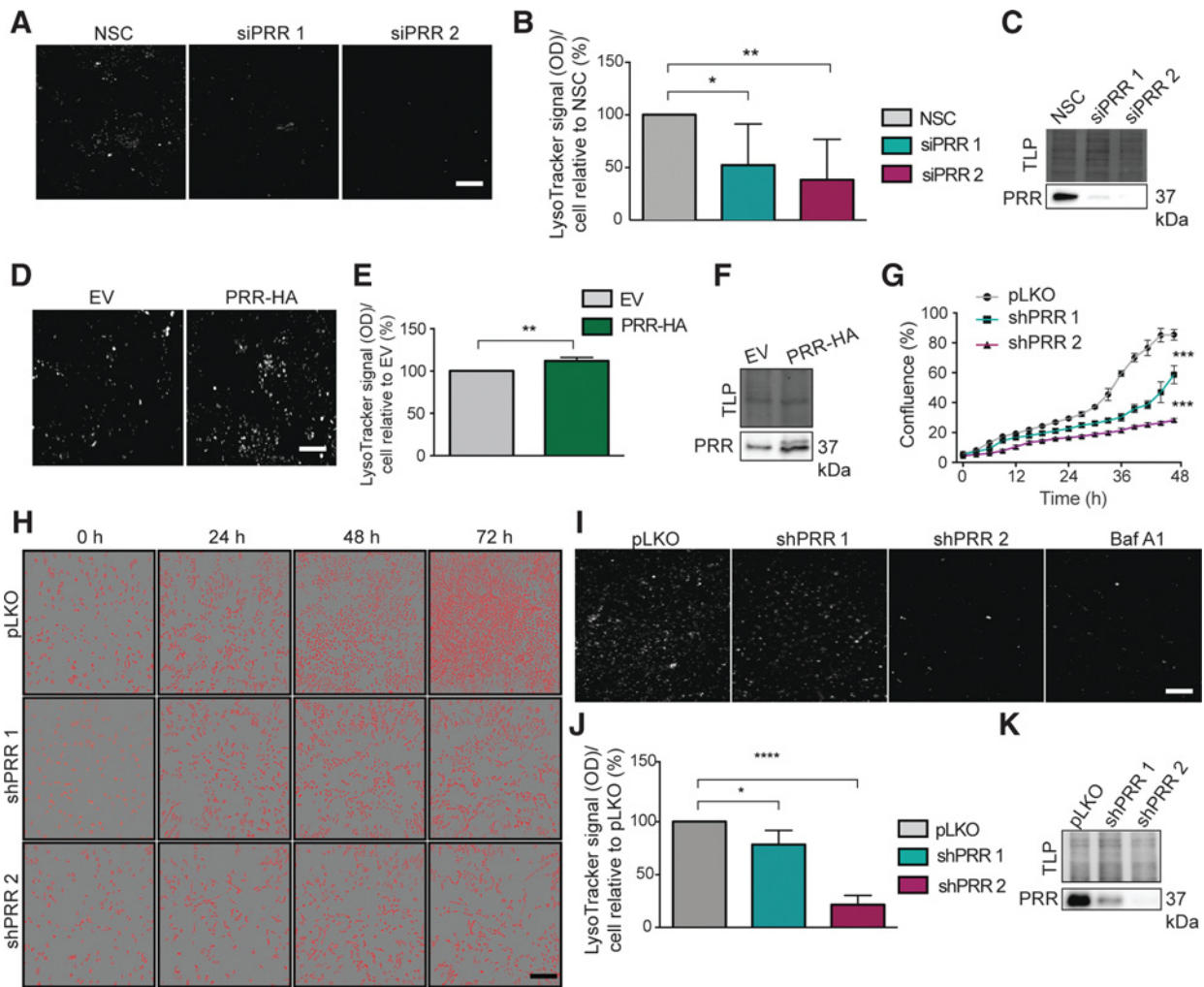


Figure 3. PRR expression enhances V-ATPase complex function and cell growth. **A**, Representative LysoTracker images of MCF-7 cells transfected with nonsilencing control (NSC), or two different siRNAs targeting PRR (siPRR 1 and 2). **B**, Corresponding quantification of LysoTracker signal in MCF-7 cells transfected with NSC, siPRR 1, and siPRR 2 ($n = 3$). **C**, Western blot analysis confirming PRR knockdown efficiency in MCF-7 cells. **D**, Representative LysoTracker images of MCF-7 cells transfected with a vector pcDNA3-HA (EV) or with PRR-pcDNA3 (PRR-HA). **E**, Corresponding quantification of LysoTracker signal per cell after overexpression of PRR protein relative to EV ($n = 3$). **F**, Western blot analysis confirming expression of PRR-HA in MCF-7 cells. **G**, Proliferation curves of MDA-MB 231 cells after stable PRR knockdown using two different PRR shRNAs: PRR shRNA 1 (shPRR 1) and PRR shRNA 2 (shPRR 2; $n = 4$). **H**, Representative brightfield images of MDA-MB 231 cells stably infected with empty pLKO vector, shPRR 1, and shPRR 2 over 1, 2, and 3 days (magnification, 10 \times ; scale bar, 250 μ m). **I**, Representative LysoTracker images of MDA-MB 231 cells infected with pLKO vector, shPRR 1, shPRR 2, or treated with Bafilomycin A1 (Baf A1; 100 nmol/L). **J**, Corresponding quantification of LysoTracker signal per MDA-MB 231 cell after PRR knockdown with shPRR 1 and shPRR 2 relative to pLKO ($n = 3$). **K**, Western blot analysis of PRR confirming knockdown of PRR after stable infection with lentivirus-expressing shPRR 1 and shPRR 2 in MDA-MB 231 cells, compared with infection with pLKO vector. Scale bar, 100 μ m on 20 \times images for LysoTracker images. Corresponding brightfield images for LysoTracker fields can be found in Supplementary Fig. S2. TLP, total lane protein; *, $P \leq 0.05$; **, $P \leq 0.01$; ***, $P \leq 0.005$; ****, $P < 0.0001$.

and *PTEN*sh MCF-7 cells and measured V-ATPase activity. Interestingly, PRR knockdown reversed the increase in V-ATPase activity observed after *PTEN* knockdown (Fig. 2D–H; Supplementary Fig. S2B and S2C). Taken together, these observations demonstrate a direct link between *PTEN* levels and V-ATPase complex activity that is mediated by expression of PRR (Fig. 2I).

PRR expression enhances V-ATPase complex function and cell growth

To further assess the relationship between PRR expression and V-ATPase activity, PRR was knocked down in MCF-7 cells and changes

in intracellular acidification were assayed by LysoTracker staining. PRR knockdown in MCF-7 cells resulted in a significant reduction in acidification (Fig. 3A–C; Supplementary Fig. S2D). Conversely, overexpression of PRR in MCF-7 cells led to an elevated LysoTracker signal (Fig. 3D–F; Supplementary Fig. S2E). We then tested the effect of PRR knockdown on the growth of MDA-MB 231 cells, which are particularly fast-growing breast cancer lines. Stable knockdown of PRR in these cells resulted in a significant decrease in cell proliferation (Fig. 3G and H). Similar to MCF-7 cells, knockdown of PRR in MDA-MB 231 cells resulted in a decreased LysoTracker signal (Fig. 3I–K; Supplementary Fig. S2F). These results show that

modulation of PRR expression affects both V-ATPase activity and cell growth in breast cancer cells.

PRR gene (*ATP6AP2*) expression is elevated in breast cancer, and sPRR concentration in patient plasma correlates with tumor burden in HER2-enriched cancer

The relationship between PRR, PTEN, and V-ATPase activity prompted us to examine PRR expression and sPRR secretion in clinical samples. First, IHC for PRR/sPRR was performed on 166 breast cancer sections using a TMA (Supplementary Table S1A). Phospho-Akt (P-Akt) was also stained as a marker for PI3K pathway activity (Fig. 4A; Supplementary Table S1B). Tumors were grouped on the basis of estrogen receptor (ER), progesterone receptor (PR), and HER2 status and mean PRR/sPRR staining scores were determined for each combination to investigate association between PRR/sPRR staining and receptor status. The combinations ER⁺/PR⁻/HER2⁺ and ER⁺/PR⁻/HER2⁻ were excluded from the analysis due to the low numbers of these tumors. No significant differences were observed for PRR/sPRR staining among the receptor combinations (Fig. 4B). P-Akt staining had the highest score in the ER⁻/PR⁻/HER2⁺ patient TMAs compared with other receptor combinations (Fig. 4C), as reported previously (42). There was also no correlation between PRR/sPRR and P-Akt staining scores (Supplementary Fig. S3A). We further looked for relationships between parameters of patient outcome and PRR/sPRR staining and observed no significant correlations (Supplementary Fig. S3B–S3D).

Because the N-terminal fragment of PRR, sPRR, is secreted, we next determined whether sPRR concentration was elevated in the plasma of patients with breast cancer relative to healthy subjects (Supplementary Table S2). We observed a significant increase of sPRR concentration in all of the breast cancer subtypes with the exception of HER2-enriched tumors (Fig. 4D). Interestingly, when we assessed the correlation between tumor volume and sPRR levels, there was a positive correlation only in the HER2-enriched subtype (Fig. 4E–H). However, blood sPRR levels did not correlate with lymph node involvement (Supplementary Fig. S3E), or with recurrence (Supplementary Fig. S3F).

LCM allows extraction of mRNA from a specific morphologically distinctive population of cells. Analysis of *ATP6AP2* and *PTEN* gene expression were analyzed in breast normal epithelial, tumor epithelial, tumor stromal, and normal stromal cells. Higher levels of PRR mRNA were observed in Basal, HER2-enriched, and Luminal A tumor epithelial cells compared with normal epithelial cells (Fig. 4I). However, there was no difference in the levels of PRR mRNA between normal and tumor stromal cells, which shows that the increase in PRR mRNA is specific to the epithelia (Fig. 4I). For *PTEN* mRNA levels, there was no difference between normal and tumor epithelial cells among the different subtypes (Fig. 4J). Nonetheless, we observed higher levels of *PTEN* mRNA in stromal cells surrounding HER2-enriched, Luminal A, and Luminal B tumors when compared with stromal cells in normal breast tissue (Fig. 4J). Furthermore, using TCGA datasets, we noted a significant increase in *ATP6AP2* gene expression in Luminal A and Luminal B subtypes compared with Basal-like breast cancer subtype (Fig. 4K).

We then classified patients on the basis of “high” and “low” *ATP6AP2* mRNA levels and examined recurrence-free survival in the different subtypes. Basal and HER2 breast cancer subtype patients with “high” PRR mRNA levels showed a pattern of reduced recurrence-free survival when compared with “low” PRR mRNA level patients (Supplementary Fig. S3G and S3H). Luminal A and

Luminal B subtype patients demonstrated no distinctive pattern of decreasing recurrence-free survival between the “low” and “high” *ATP6AP2* patient groups (Supplementary Fig. S3I and S3J). Overall, the clinical data indicate that PRR expression is elevated in breast cancer tissue with emphasis on the role of PRR in HER2-enriched cancer.

PRR expression is required to maintain HER2 expression and signaling

The positive correlation between sPRR plasma concentration and tumor volume in HER2-enriched patients prompted us to further investigate the role of PRR in HER2 signaling. To test the effect of PRR on HER2 expression and signaling, PRR was knocked down in three HER2-positive breast cancer cell lines: SKBR3, MDA-MB 361, and MDA-MB 893. Knockdown of PRR had no effect on the phosphorylation of HER2, but reduced HER2 expression in SKBR3 and MDA-MB 893 cell lines (Fig. 5A–G). The same PRR knockdown effect on HER2 expression was not observed in MDA-MB 361 cells, pointing at the variability in HER2 expression (Fig. 5B, and E–G). In SKBR3 and MDA-MB 893 cells, Akt phosphorylation and p44/42 MAPK phosphorylation were reduced as a result of PRR knockdown (Fig. 5A–G), suggesting that HER2 downstream signaling may be dampened as a result of PRR knockdown. To further examine the effect of PRR on HER2 expression, we tested HER2 localization after PRR knockdown using immunofluorescence in SKBR3 and MDA-MB 893 cells. PRR knockdown significantly reduced the staining intensity of HER2 receptor in both cell lines (Fig. 6A–E; Supplementary Fig. S2G). Inhibition of the V-ATPase complex using Bafilomycin A1 had a similar effect on HER2 expression (Fig. 6A–E). PRR knockdown also reduced the membranous localization of HER2 indicating that loss of PRR expression may interfere with normal endosomal trafficking and recycling of HER2 (Fig. 6F–I; Supplementary Fig. S2G). Together, these findings suggest that PRR and its effects on V-ATPase activity are required for normal HER2 localization and signaling.

PRR knockdown downregulates mTORC1 activity in HER2-positive breast cancer cells

Because the V-ATPase complex has a pivotal role in mTORC1 signaling, we next investigated the effect of PRR knockdown on this pathway in HER2-positive SKBR3 and MDA-MB 893 cells. PRR knockdown caused a significant reduction in p70S6K phosphorylation (Fig. 7A and B). Also, PRR knockdown caused a downward shift ($\gamma \rightarrow \beta \rightarrow \alpha$) in the phosphorylation pattern of residues threonine 37 and 46, and significantly reduced the phosphorylation of serine 65 on 4E binding protein 1 (4EBP1; Fig. 7A and C). Both PRR knockdown and trastuzumab treatment resulted in significantly reducing polysome levels compared with nonsilencing control indicating that the rate of mRNA translation is dampened following PRR knockdown and trastuzumab treatment (Fig. 7D and E). In MDA-MB 893 cells, PRR knockdown also reduced phosphorylation of p70S6K and 4EBP1 (Fig. 7F–H), and polysome levels (Fig. 7I and J) to a similar degree as trastuzumab treatment. Together, these observations suggest that PRR is required for optimal mTORC1 activation in HER2-positive cells.

Discussion

In this study, we show a connection between PTEN expression and V-ATPase complex activity. Moreover, the functional link between PTEN and the V-ATPase complex appears to be mediated by expression of PRR, which is regulated by PTEN. Our data also reveals a

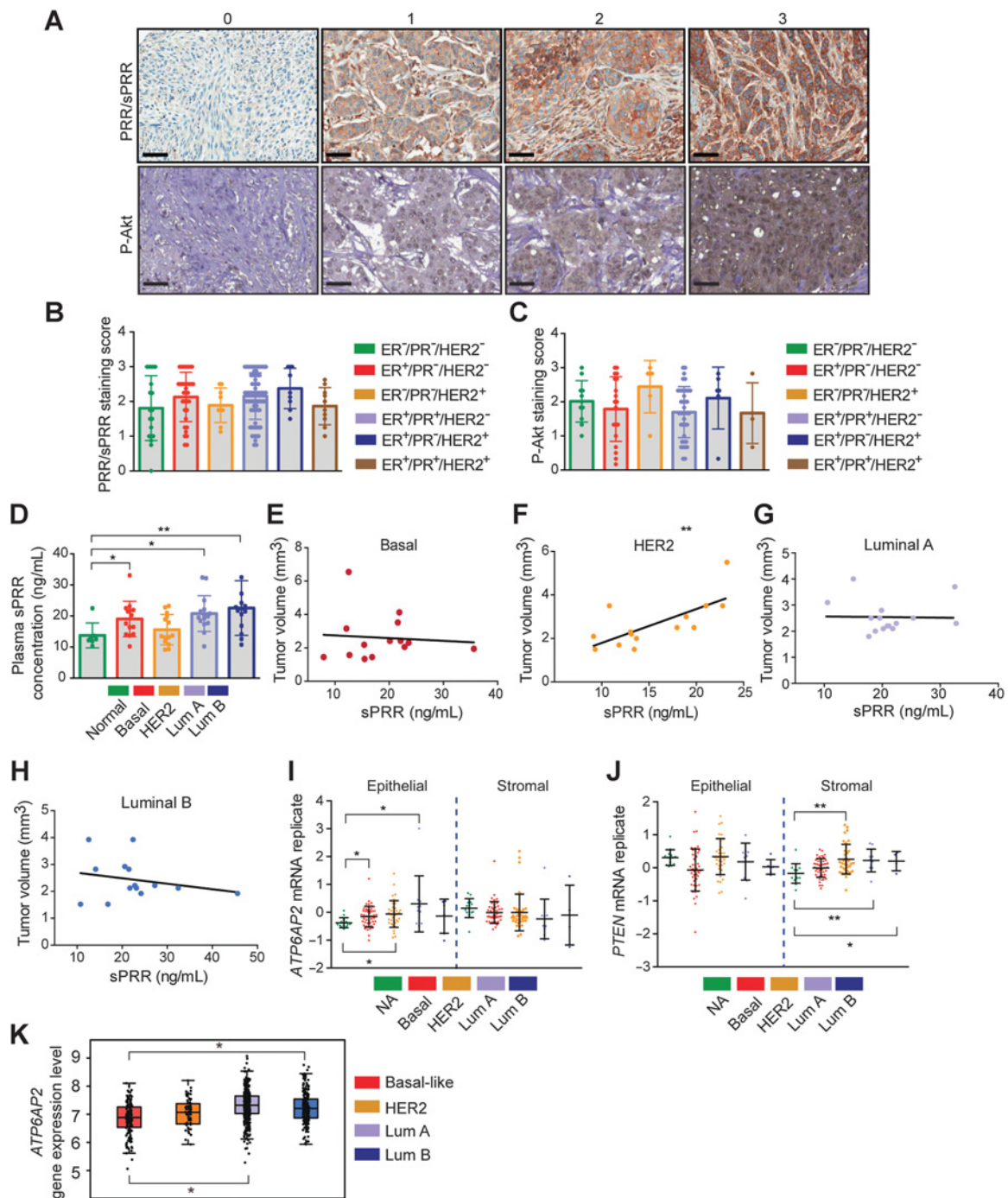


Figure 4. PRR gene (*ATP6AP2*) expression is elevated in breast cancer and sPRR concentration in patient plasma correlates with tumor burden in HER2-enriched cancer. **A**, Representative images of breast cancer sections with staining scores of 0, 1, 2, and 3 for PRR/sPRR (top) and P-Akt (bottom; magnification, 100 ×; scale bar, 50 μm). Scatter bar graphs showing the mean. PRR/sPRR (**B**) and P-Akt (**C**) staining scores across the different receptor combinations of ER⁻/PR⁻/HER2⁻ (PRR, *n* = 19; P-Akt, *n* = 11), ER⁺/PR⁻/HER2⁻ (PRR, *n* = 33; P-Akt, *n* = 19), ER⁻/PR⁺/HER2⁺ (PRR, *n* = 9; P-Akt, *n* = 6), ER⁺/PR⁺/HER2⁻ (PRR, *n* = 71; P-Akt, *n* = 39), ER⁺/PR⁻/HER2⁺ (PRR, *n* = 9; P-Akt, *n* = 6), and ER⁺/PR⁺/HER2⁺ (PRR, *n* = 10; P-Akt, *n* = 4). **D**, Scatter bar graph of ELISA showing concentration of sPRR in plasma of patients with breast cancer and in healthy female controls (*n* = 7), Basal (*n* = 17), HER2-enriched (*n* = 14), Luminal A (*n* = 15), and Luminal B (*n* = 14) subtypes. Scatterplots of breast tumor volume and sPRR concentration in Basal (*r* = -0.08; *n* = 17; **E**), HER2-enriched (*r* = 0.71; **, *P* = 0.004; *n* = 14; **F**), Luminal A (*r* = -0.02; *n* = 15; **G**), and Luminal B (*r* = -0.24; *n* = 14; **H**) subtypes. Column scatterplots of PRR (**I**) and PTEN (**J**) mRNA levels assessed in LCM epithelial and stromal cells from normal adjacent tissue (NA; *n* = 14) and from breast cancer tissues of Basal (*n* = 46), HER2-enriched (*n* = 36), Luminal A (*n* = 10), and Luminal B (*n* = 6) subtypes. **K**, Scatter whisker and box plots demonstrating levels of *ATP6AP2* gene expression from TCGA dataset using RSEM normalized count in Basal-like (*n* = 135), HER2 (*n* = 66), Luminal A (*n* = 415), and Luminal B (*n* = 194). Lum A, Luminal A; Lum B, Luminal B. *, *P* ≤ 0.05; **, *P* ≤ 0.01.

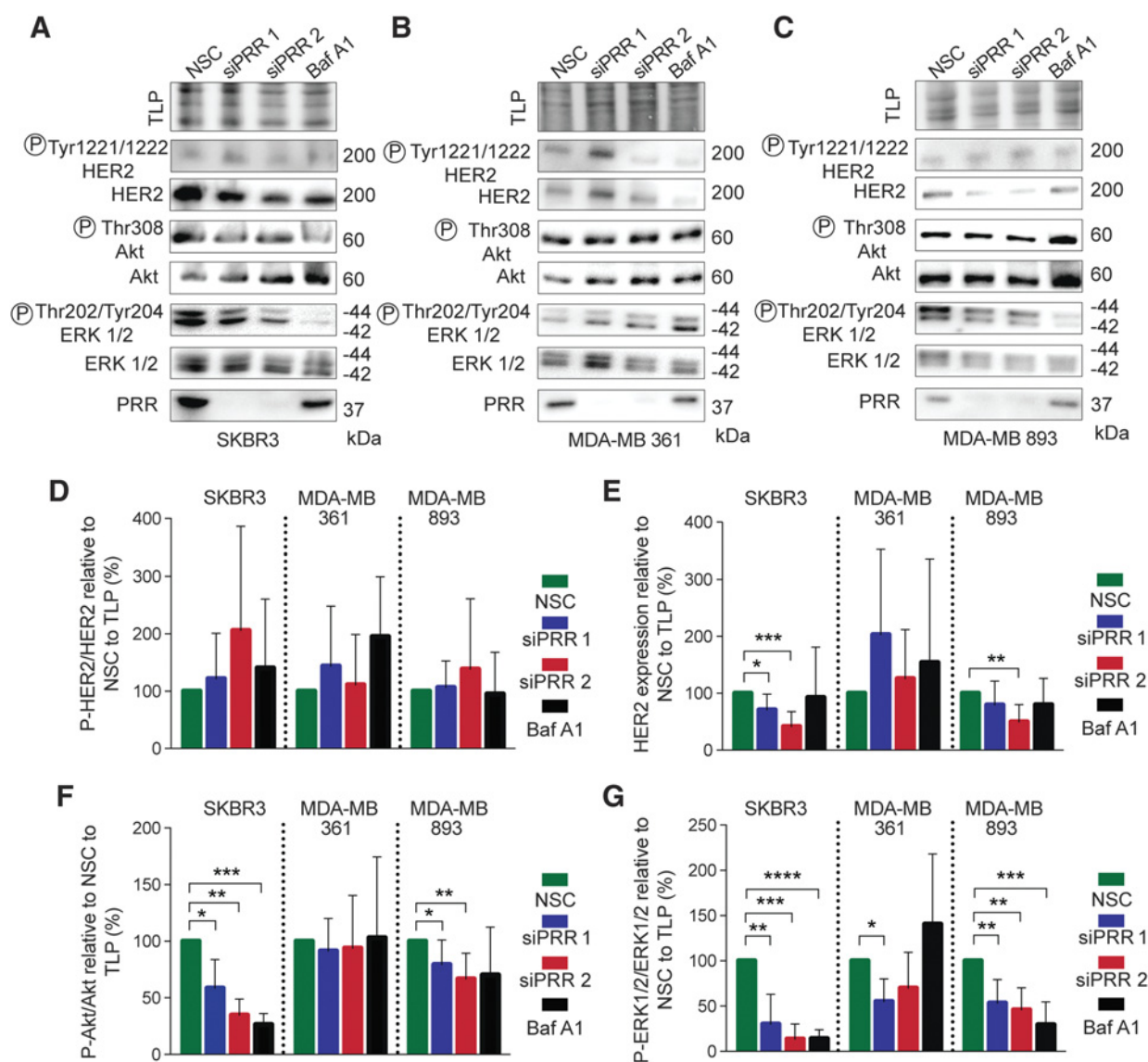


Figure 5. PRR expression is required to maintain HER2 expression and signaling. Western blot analysis of phospho-HER2 (P-HER2), total HER2, phospho-Akt (P-Akt), total Akt, phospho-p44/42 MAPK (P-ERK1/2), total p44/42 MAPK (ERK1/2), and PRR in HER2-positive SKBR3 (A), MDA-MB 361 (B), and MDA-MB 893 (C) cells transfected with nonsilencing control siRNA (NSC) or two different siRNAs targeting PRR (siPRR1 and 2) or treated with Bafilomycin A1 (Baf A1; 100 nmol/L). Corresponding band quantification of P-HER2 relative to total HER2 levels (D), HER2 protein expression (E), P-Akt relative to total Akt levels (F), and p-ERK1/2 relative to total ERK1/2 (G) in SKBR3 ($n = 7$), MDA-MB 361 ($n = 5$), and MDA-MB 893 ($n = 6$) following PRR knockdown. Treatment with Bafilomycin A1 is included as a positive control for V-ATPase inhibition. TLP, total lane protein; *, $P \leq 0.05$; **, $P \leq 0.01$; ***, $P \leq 0.005$; ****, $P < 0.0001$.

positive correlation between sPRR levels and tumor burden only in HER2-positive patients. In HER2-enriched cells, we show that PRR levels dictate HER2 signaling, expression, and localization. Furthermore, PRR expression is required for effective mTORC1 signaling in HER2-positive cells. Overall, our study provides evidence for the involvement of PRR in multiple oncogenic pathways in breast cancer.

Levels of sPRR were increased in the blood of all breast cancer subtype patients except the HER2-enriched subtype. However, positive correlation between tumor volume and sPRR concentration could only be established for HER2-enriched patients. HER2-positive cells may selectively benefit from the role of PRR within the cell and the data

we present here demonstrate that PRR expression is important for proper HER2 expression, localization, and downstream signaling. PRR is likely required to maintain proper HER2 trafficking by promoting V-ATPase complex formation, and endosomal acidification and receptor recycling. Therefore, intracellular retention of the unprocessed form of PRR may be favorable for the oncogenesis of HER2-positive breast cancer cells.

Although the effect of PRR knockdown on HER2 localization and signaling was evident in SKBR3 and MDA-MB 893 cells, the same effect could not be demonstrated in MDA-MB 361 cells. HER2 in MDA-MB 361 cells may be more stable due to selective binding of

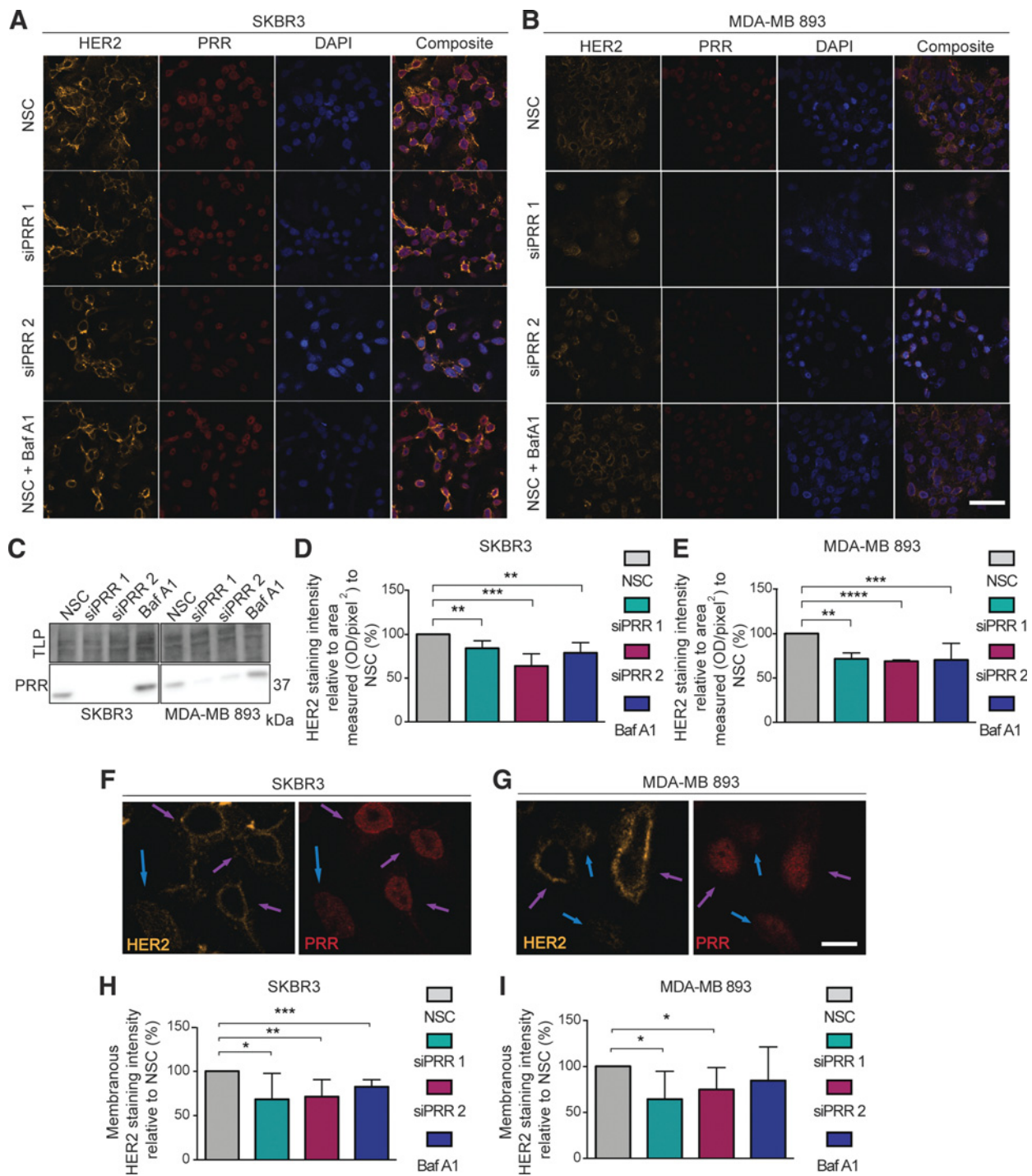


Figure 6.

HER2 expression and cellular localization after PRR knockdown. Immunofluorescence images of HER2, PRR, and DAPI in HER2-positive SKBR3 (**A**) and MDA-MB 893 (**B**) after transfection with nonsilencing control siRNA (NSC), or two different siRNAs targeting PRR (siPRR 1 and 2) or treatment with Bafilomycin A1 (Baf A1; 100 nmol/L), as a positive control for V-ATPase inhibition (magnification, 40 \times ; scale bar, 60 μ m). **C**, Western blot analysis of PRR expression indicating effective PRR knockdown following transfection with siPRR 1 and siPRR 2. Corresponding quantification of HER2 signal in SKBR3 (**D**) and MDA-MB 893 (**E**) following PRR knockdown with siPRR 1 or siPRR 2 and Bafilomycin A1 ($n = 4$). Representative images of SKBR3 (**F**) and MDA-MB 893 (**G**) cells showing the correlation between PRR expression and HER2 localization. Purple arrows indicate cells with membrane-localized HER2 and blue arrows indicate cells with cytoplasmic HER2 localization. Cells with low PRR expression consistently lack membrane-localized HER2 (magnification, 63 \times ; scale bar, 12 μ m). Corresponding quantification of percentage of cells with membranous HER2 localization in SKBR3 (**H**) and MDA-MB 893 (**I**) after PRR knockdown using siPRR 1, siPRR 2, or treatment with Bafilomycin A1 ($n = 3$). TLP, total lane protein; *, $P \leq 0.05$; **, $P \leq 0.01$; ***, $P \leq 0.005$; ****, $P < 0.0001$.

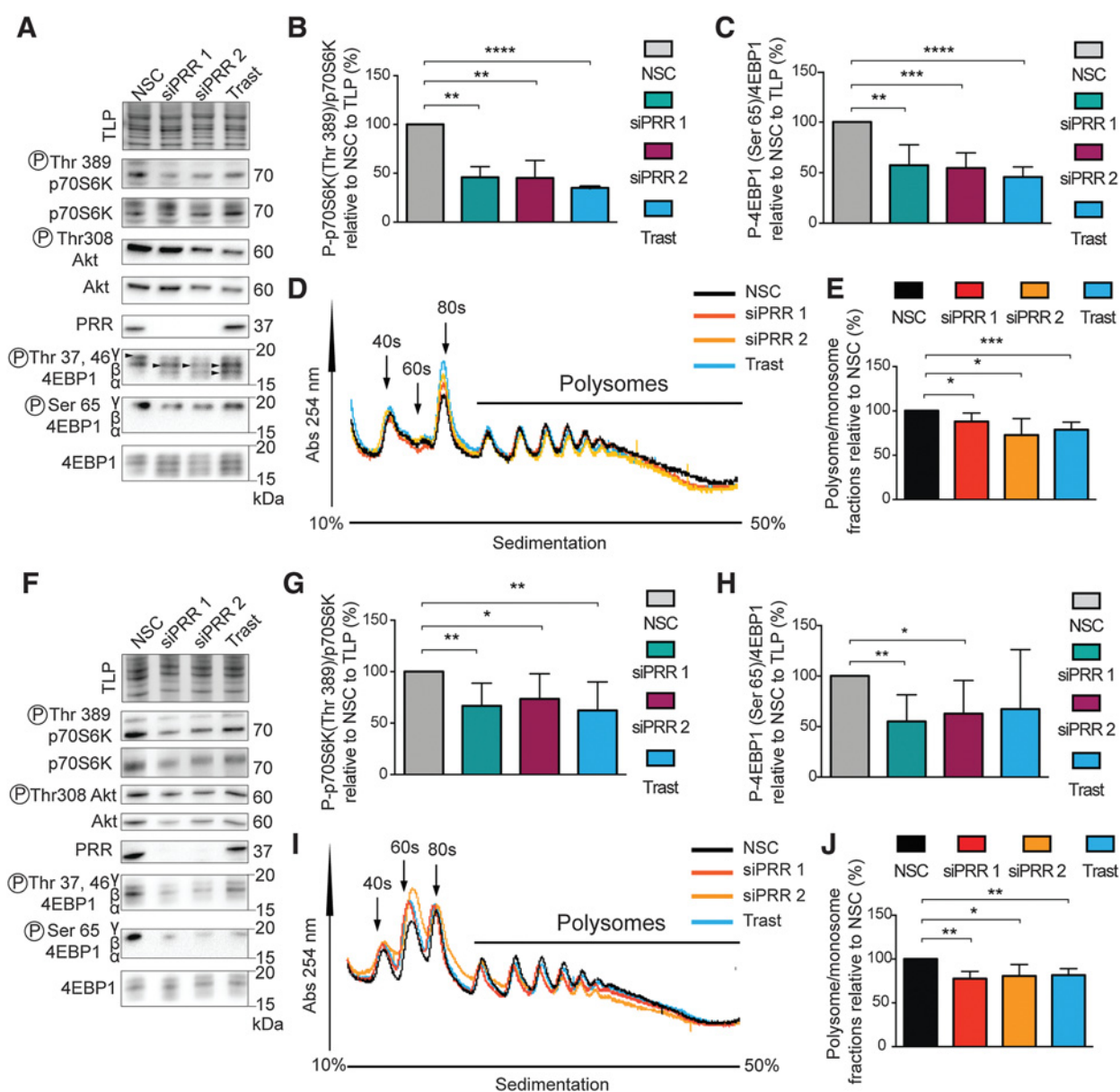


Figure 7. PRR knockdown and trastuzumab treatment reduce mTORC1 activity. **A**, Western blot analysis of phospho-Thr 389-p70S6 kinase (Thr 389 P-p70S6K), total p70S6 kinase (p70S6K), phospho-Thr 308-Akt (Thr 308 P-Akt), total Akt (Akt), PRR, phospho-Thr 37, 46-4E binding protein 1 (Thr 37, 46 P-4EBP1), phospho-Ser 65-4EBP1 (Ser 65 P-4EBP1), and total 4EBP1 after transfection with nonsilencing control (NSC), or two different siRNAs targeting PRR (siPRR 1 and 2) in SKBR3 cells. Treatment with trastuzumab (Trast; 100 nmol/L) is included as a positive control for HER2 inhibition. **B**, Quantification of Thr 389 P-p70S6K relative to p70S6K after PRR knockdown using siPRR 1, siPRR 2, or treatment with trastuzumab in SKBR3 cells ($n = 5$). **C**, Quantification of Ser 65 P-4EBP1 relative to 4EBP1 after PRR knockdown using siPRR 1, siPRR 2, or treatment with trastuzumab in SKBR3 cells ($n = 5$). **D**, Representative polysome profiles of SKBR3 cells transfected with NSC, siPRR 1, siPRR 2, or treated with trastuzumab in SKBR3 cells. **E**, Quantification of the ratio of polysome to monosome translation after PRR knockdown using siPRR1, siPRR2, or treatment with trastuzumab in SKBR3 cells ($n = 5$). **F**, Western blot analysis of Thr 389 P-p70S6K kinase, p70S6K, Thr 308 P-Akt, Akt, PRR, Thr 37, 46 P-4EBP1, Ser 65 P-4EBP1, and 4EBP1 after transfecting MDA-MB 893 cells with NSC, siPRR 1, siPRR 2, or treatment with trastuzumab. **G**, Quantification of Thr 389 P-p70S6K relative to p70S6K after PRR knockdown using siPRR 1, siPRR 2, or treatment with trastuzumab in MDA-MB 893 cells ($n = 5$). **H**, Quantification of Ser 65 P-4EBP1 relative to 4EBP1 after PRR knockdown using siPRR 1, siPRR 2, or treatment with trastuzumab in MDA-MB 893 cells ($n = 5$). **I**, Representative polysome profiles of MDA-MB 893 cells transfected with NSC, siPRR 1, siPRR 2, or treatment with trastuzumab. **J**, Quantification of the ratio of polysome to monosome translation after PRR knockdown using siPRR1, siPRR2, or treatment with trastuzumab in MDA-MB 893 cells ($n = 4$). TLP, total lane protein; *, $P \leq 0.05$; **, $P \leq 0.01$; ***, $P \leq 0.005$; ****, $P < 0.0001$.

HER2 with other proteins. Alternatively, MDA-MB 361 cells may be less reliant on HER2 signaling than SKBR3 and MDA-MB 893 cells.

The V-ATPase complex on the lysosomal surface is directly involved in sensing amino acids within the lysosome (16). Amino

acid availability within the lysosome and the presence of growth factors at the plasma membrane activate two signaling arms that eventually initiate translation (43). Because PRR is essential for V-ATPase function, it may also be required for amino acid sensing, which may

explain the attenuation of mTORC1 signaling following PRR knockdown that we observed. The decrease in polysome translation observed after PRR knockdown is similar to the effect observed after mTOR inhibition using rapamycin (44). Autophagy is also regulated downstream of mTORC1 and it would be interesting to determine whether PRR expression also modulates this process (45). Although our study focused on the role of PRR in HER2 and mTORC1 signaling, there are other potential pathways that can be affected by PRR and the V-ATPase complex in breast cancer. For example, PRR is required for β -Catenin signaling (14, 15). Binding of Wnt ligands to frizzled/low density lipoprotein (LRP) receptor complex induces release of β -Catenin through glycogen synthase kinase (GSK-3) disassembly. It was demonstrated that the N-terminal domain of PRR connects LRP to the V-ATPase complex.

PRR and the V-ATPase may also mediate changes in the micro-environment in breast cancer. Localization of the V-ATPase complex at the growing edge of tumors has been observed (46, 47), suggesting that V-ATPase-mediated acidification may be partly responsible for extracellular matrix remodeling and tumor expansion. This notion is supported by evidence showing that V-ATPase complex subunit expression correlates with cell line invasiveness and metastatic potential (48).

We observe that loss of PTEN results in elevated expression of the *ATP6AP2* gene both *in vitro* and *in vivo*. It remains unclear how loss of PTEN leads to transcriptional upregulation of the *ATP6AP2* gene. PTEN regulation of *ATP6AP2* gene may involve transcription factors downstream of the PI3K pathway. Consistent with this notion, V-ATPase subunit expression and activity were demonstrated to be upregulated via mTORC1 regulation of the transcription factor TFEB, which may explain how PTEN loss increases *ATP6AP2* expression (49).

Our data also indicate that PTEN may regulate PRR processing independently of PRR expression levels. PRR is processed at the R-X-X-R motif, which is recognized by endoproteases of the proprotein convertase (PC) family (22). Among others, the PC family includes PACE4, furin, and PC7. The possible cleavage of PRR by other proteases, such as ADAM 19 (50), can explain our observation of doublet bands for sPRR in Fig. 1. It remains unclear whether PRR processing is necessary for the function PRR plays with the V-ATPase complex. At least one study reported an inverse relationship between expressions of PTEN and furin (51). In addition, another study showed that PACE4 enhances proliferation of ER⁺ breast cancer cells (52). Therefore, PTEN may control PRR processing by regulating expression of PC members responsible for cleaving PRR.

References

1. Cancer Genome Atlas Network. Comprehensive molecular portraits of human breast tumours. *Nature* 2012;490:61–70.
2. Carracedo A, Alimonti A, Pandolfi PP. PTEN level in tumor suppression: how much is too little? *Cancer Res* 2011;71:629–33.
3. Mayer IA, Arteaga CL. The PI3K/AKT pathway as a target for cancer treatment. *Annu Rev Med* 2016;67:11–28.
4. Schade B, Rao T, Dourdin N, Lesurf R, Hallett M, Cardiff RD, et al. PTEN deficiency in a luminal ErbB-2 mouse model results in dramatic acceleration of mammary tumorigenesis and metastasis. *J Biol Chem* 2009;284:19018–26.
5. Nagata Y, Lan KH, Zhou X, Tan M, Esteva FJ, Sahin AA, et al. PTEN activation contributes to tumor inhibition by trastuzumab, and loss of PTEN predicts trastuzumab resistance in patients. *Cancer Cell* 2004;6:117–27.
6. Berns K, Horlings HM, Hennessy BT, Madiredjo M, Hijmans EM, Beelen K, et al. A functional genetic approach identifies the PI3K pathway as a major determinant of trastuzumab resistance in breast cancer. *Cancer Cell* 2007;12:395–402.
7. Dave B, Migliaccio I, Gutierrez MC, Wu MF, Chamness GC, Wong H, et al. Loss of phosphatase and tensin homolog or phosphoinositide-3 kinase activation and response to trastuzumab or lapatinib in human epidermal growth factor receptor 2-overexpressing locally advanced breast cancers. *J Clin Oncol* 2011;29:166–73.
8. Kohio HP, Adamson AL. Glycolytic control of vacuolar-type ATPase activity: a mechanism to regulate influenza viral infection. *Virology* 2013;444:301–9.
9. Marjuki H, Gornitzky A, Marathe BM, Ilyushina NA, Aldridge JR, Desai G, et al. Influenza A virus-induced early activation of ERK and PI3K mediates V-ATPase-dependent intracellular pH change required for fusion. *Cell Microbiol* 2011;13:587–601.
10. Sautin YY, Lu M, Gaugler A, Zhang L, Gluck SL. Phosphatidylinositol 3-kinase-mediated effects of glucose on vacuolar H⁺-ATPase assembly, translocation, and acidification of intracellular compartments in renal epithelial cells. *Mol Cell Biol* 2005;25:575–89.

Disclosure of Potential Conflicts of Interest

No potential conflicts of interest were disclosed.

Authors' Contributions

A.H. Mohammad: Conceptualization, data curation, formal analysis, validation, writing-original draft, writing-review and editing. S.-H. Kim: Data curation. N. Bertos: Resources. W. El-Asaad: Data curation. I. Nandi: Resources, methodology. H. Smith: Resources. J. Yang: Conceptualization, data curation. O.J. Chen: Data curation. I. Gamache: Resources. T. Rao: Resources. B. Gagnon: Resources. T. Gruosso: Resources, software, methodology. M.L. Tremblay: Supervision. N. Sonenberg: Supervision. M.-C. Guiot: Data curation, supervision. W. Muller: Supervision. M. Park: Supervision. J.G. Teodoro: Conceptualization, supervision, funding acquisition, validation, investigation, methodology, writing-original draft, project administration, writing-review and editing.

Acknowledgments

This work was supported by grants from the Canadian Institutes of Health Research (CIHR), and Cancer Research Society (to J.G. Teodoro). A.H. Mohammad was a recipient of a Vanier Scholarship from the CIHR. This work was partially supported by a grant from the Terry Fox Research Institute, Canada (to B. Gagnon and M.L. Tremblay). We thank Chris Kontos for the Ad-PTEN. We thank Genentech for supplying trastuzumab. We also thank the Canadian Centre for Computational Genomics (C3G) for their help with the bioinformatic analysis. The breast tissue bank and databank at the Research Institute of the McGill University Health Centre was supported by funding from the Database and Tissue Bank Axis of the Réseau de Recherche en Cancer of the Fonds de Recherche du Québec-Santé and the Québec Breast Cancer Foundation. This work was supported by CIHR, Prostate Cancer Canada.

The costs of publication of this article were defrayed in part by the payment of page charges. This article must therefore be hereby marked *advertisement* in accordance with 18 U.S.C. Section 1734 solely to indicate this fact.

Received January 26, 2020; revised April 30, 2020; accepted June 18, 2020; published first June 25, 2020.

11. Xu Y, Parmar A, Roux E, Balbis A, Dumas V, Chevalier S, et al. Epidermal growth factor-induced vacuolar (H⁺)-ATPase assembly: a role in signaling via mTORC1 activation. *J Biol Chem* 2012;287:26409–22.
12. Sun-Wada GH, Wada Y. Role of vacuolar-type proton ATPase in signal transduction. *Biochim Biophys Acta* 2015;1847:1166–72.
13. Aster JC, Pear WS, Blacklow SC. The varied roles of notch in cancer. *Annu Rev Pathol* 2017;12:245–75.
14. Cruciat CM, Ohkawara B, Acebron SP, Karaulanov E, Reinhard C, Ingelfinger D, et al. Requirement of prorenin receptor and vacuolar H⁺-ATPase-mediated acidification for Wnt signaling. *Science* 2010;327:459–63.
15. Hermle T, Saltukoglu D, Grunewald J, Walz G, Simons M. Regulation of Frizzled-dependent planar polarity signaling by a V-ATPase subunit. *Curr Biol* 2010;20:1269–76.
16. Zoncu R, Bar-Peled L, Efeyan A, Wang S, Sancak Y, Sabatini DM. mTORC1 senses lysosomal amino acids through an inside-out mechanism that requires the vacuolar H⁽⁺⁾-ATPase. *Science* 2011;334:678–83.
17. Kozik P, Hodson NA, Sahlender DA, Simecek N, Soromani C, Wu J, et al. A human genome-wide screen for regulators of clathrin-coated vesicle formation reveals an unexpected role for the V-ATPase. *Nat Cell Biol* 2013;15:50–60.
18. Forgac M. Vacuolar ATPases: rotary proton pumps in physiology and pathophysiology. *Nat Rev Mol Cell Biol* 2007;8:917–29.
19. Marshansky V, Futai M. The V-type H⁺-ATPase in vesicular trafficking: targeting, regulation and function. *Curr Opin Cell Biol* 2008;20:415–26.
20. von Schwarzenberg K, Lajtos T, Simon L, Muller R, Vereb G, Vollmar AM. V-ATPase inhibition overcomes trastuzumab resistance in breast cancer. *Mol Oncol* 2014;8:9–19.
21. Mohammad AH, Assadian S, Couture F, Lefebvre KJ, El-Assaad W, Barres V, et al. V-ATPase-associated prorenin receptor is upregulated in prostate cancer after PTEN loss. *Oncotarget* 2019;10:4923–36.
22. Cousin C, Bracquart D, Contrepas A, Corvol P, Muller L, Nguyen G. Soluble form of the (pro)renin receptor generated by intracellular cleavage by furin is secreted in plasma. *Hypertension* 2009;53:1077–82.
23. Nguyen G. Renin, (pro)renin and receptor: an update. *Clin Sci* 2011;120:169–78.
24. Biswas KB, Nabi AN, Arai Y, Nakagawa T, Ebihara A, Ichihara A, et al. Qualitative and quantitative analyses of (pro)renin receptor in the medium of cultured human umbilical vein endothelial cells. *Hypertens Res* 2011;34:735–9.
25. Ludwig J, Kerscher S, Brandt U, Pfeiffer K, Getlawi F, Apps DK, et al. Identification and characterization of a novel 9.2-kDa membrane sector-associated protein of vacuolar proton-ATPase from chromaffin granules. *J Biol Chem* 1998;273:10939–47.
26. Advani A, Kelly DJ, Cox AJ, White KE, Advani SL, Thai K, et al. The (Pro)renin receptor: site-specific and functional linkage to the vacuolar H⁺-ATPase in the kidney. *Hypertension* 2009;54:261–9.
27. Kinouchi K, Ichihara A, Sano M, Sun-Wada GH, Wada Y, Kurauchi-Mito A, et al. The (pro)renin receptor/ATP6AP2 is essential for vacuolar H⁺-ATPase assembly in murine cardiomyocytes. *Circ Res* 2010;107:30–4.
28. Oshima Y, Kinouchi K, Ichihara A, Sakoda M, Kurauchi-Mito A, Bokuda K, et al. Prorenin receptor is essential for normal podocyte structure and function. *J Am Soc Nephrol* 2011;22:2203–12.
29. Nguyen G, Delarue F, Burckle C, Bouzahir L, Giller T, Sraer JD. Pivotal role of the renin/prorenin receptor in angiotensin II production and cellular responses to renin. *J Clin Invest* 2002;109:1417–27.
30. Burckle C, Bader M. Prorenin and its ancient receptor. *Hypertension* 2006;48:549–51.
31. Wendling O, Champy MF, Jaubert S, Pavlovic G, Dubos A, Lindner L, et al. Atp6ap2 ablation in adult mice impairs viability through multiple organ deficiencies. *Sci Rep* 2017;7:9618.
32. Collins MP, Forgac M. Regulation of V-ATPase assembly in nutrient sensing and function of V-ATPases in breast cancer metastasis. *Front Physiol* 2018;9:902.
33. Taylor SC, Posch A. The design of a quantitative Western blot experiment. *Biomed Res Int* 2014;2014:361590.
34. Taylor SC, Berkelman T, Yadav G, Hammond M. A defined methodology for reliable quantification of Western blot data. *Mol Biotechnol* 2013;55:217–26.
35. Groitl P, Dobner T. Construction of adenovirus type 5 early region 1 and 4 virus mutants. *Methods Mol Med* 2007;130:29–39.
36. Muller WJ, Sinn E, Pattengale PK, Wallace R, Leder P. Single-step induction of mammary adenocarcinoma in transgenic mice bearing the activated c-neu oncogene. *Cell* 1988;54:105–15.
37. Siegel PM, Ryan ED, Cardiff RD, Muller WJ. Elevated expression of activated forms of Neu/ErbB-2 and ErbB-3 are involved in the induction of mammary tumors in transgenic mice: implications for human breast cancer. *EMBO J* 1999;18:2149–64.
38. Andreichek ER, Hardy WR, Siegel PM, Rudnicki MA, Cardiff RD, Muller WJ. Amplification of the neu/erbB-2 oncogene in a mouse model of mammary tumorigenesis. *Proc Natl Acad Sci U S A* 2000;97:3444–9.
39. Li G, Robinson GW, Lesche R, Martinez-Diaz H, Jiang Z, Rozenfurt N, et al. Conditional loss of PTEN leads to precocious development and neoplasia in the mammary gland. *Development* 2002;129:4159–70.
40. Tang Z, Chen T, Ren X, Zhang Z. Identification of transcriptional isoforms associated with survival in cancer patient. *J Genet Genomics* 2019;46:413–21.
41. Finak G, Sadekova S, Pepin F, Hallett M, Meterissian S, Halwani F, et al. Gene expression signatures of morphologically normal breast tissue identify basal-like tumors. *Breast Cancer Res* 2006;8:R58.
42. Tokunaga E, Kimura Y, Oki E, Ueda N, Futatsugi M, Mashino K, et al. Akt is frequently activated in HER2/neu-positive breast cancers and associated with poor prognosis among hormone-treated patients. *Int J Cancer* 2006;118:284–9.
43. Shimobayashi M, Hall MN. Multiple amino acid sensing inputs to mTORC1. *Cell Res* 2016;26:7–20.
44. Terada N, Patel HR, Takase K, Kohno K, Nairn AC, Gelfand EW. Rapamycin selectively inhibits translation of mRNAs encoding elongation factors and ribosomal proteins. *Proc Natl Acad Sci U S A* 1994;91:11477–81.
45. Mijaljica D, Prescott M, Devenish RJ. V-ATPase engagement in autophagic processes. *Autophagy* 2011;7:666–8.
46. Cotter K, Capecchi J, Sennoune S, Huss M, Maier M, Martinez-Zaguilan R, et al. Activity of plasma membrane V-ATPases is critical for the invasion of MDA-MB 231 breast cancer cells. *J Biol Chem* 2015;290:3680–92.
47. Kulshrestha A, Katara GK, Ibrahim S, Pamarthy S, Jaiswal MK, Gilman Sachs A, et al. Vacuolar ATPase 'a2' isoform exhibits distinct cell surface accumulation and modulates matrix metalloproteinase activity in ovarian cancer. *Oncotarget* 2015;6:3797–810.
48. Sennoune SR, Bakunts K, Martinez GM, Chua-Tuan JL, Kebir Y, Attaya MN, et al. Vacuolar H⁺-ATPase in human breast cancer cells with distinct metastatic potential: distribution and functional activity. *Am J Physiol Cell Physiol* 2004;286:C1443–52.
49. Pena-Llopis S, Vega-Rubin-de-Celis S, Schwartz JC, Wolff NC, Tran TA, Zou L, et al. Regulation of TFEB and V-ATPases by mTORC1. *EMBO J* 2011;30:3242–58.
50. Yoshikawa A, Aizaki Y, Kusano K, Kishi F, Susumu T, Iida S, et al. The (pro)renin receptor is cleaved by ADAM19 in the Golgi leading to its secretion into extracellular space. *Hypertens Res* 2011;34:599–605.
51. Yang X, Wang Q, Gao Z, Zhou Z, Peng S, Chang WL, et al. Proprotein convertase furin regulates apoptosis and proliferation of granulosa cells in the rat ovary. *PLoS One* 2013;8:e50479.
52. Panet F, Couture F, Kwiatkowska A, Desjardins R, Guerin B, Day R. PACE4 is an important driver of ZR-75-1 estrogen receptor-positive breast cancer proliferation and tumor progression. *Eur J Cell Biol* 2017;96:469–75.
53. Esteve FJ, Guo H, Zhang S, Santa-Maria C, Stone S, Lanchbury JS, et al. PTEN, PIK3CA, p-AKT, and p-p70S6K status: association with trastuzumab response and survival in patients with HER2-positive metastatic breast cancer. *Am J Pathol* 2010;177:1647–56.